Nanoscale

PAPER

View Article Online
View Journal | View Issue

Cite this: *Nanoscale*, 2024, **16**, 20940

Bi-doped ruthenium oxide nanocrystal for water oxidation in acidic media†

Shiyao Chen, [a] Hai Liu,[a] Bichen Yuan,[a] Wenhai Xu,[a] Aiqing Cao,[a] Marshet Getaye Sendeku,[b] Yaping Li, *[a] Xiaoming Sun *[a] and Fengmei Wang *[a]

Received 2nd July 2024,
Accepted 14th October 2024

DOI: 10.1039/d4nr02745k

rsc.li/nanoscale

There is an urgent need to develop a cost-effective and highly efficient acidic OER catalyst to support the progress of proton exchange membrane water electrolysis technology. Ruthenium-based catalysts, which possess high activity and significantly lower cost compared to iridium-based catalysts, emerge as competitive candidates. However, their suboptimal stability constrains the wide application of RuO_2. Herein, we develop ultra-small $Bi_{0.05}Ru_{0.95}O_2$ nanocrystal with diameter of approximately 6.5 ± 0.1 nm for acidic OER. The $Bi_{0.05}Ru_{0.95}O_2$ nanocrystal electrocatalyst exhibits a low overpotential of 203.5 mV at 10 mA cm^{-2} and 300+ hour stability at a high water-splitting current density of 100 mA cm^{-2} in 0.5 M H_2SO_4 with a low decay rate of 0.44 mV h^{-1}. Density functional theory (DFT) calculation results confirmed the adsorbate evolving mechanism (AEM) occurring on $Bi_{0.05}Ru_{0.95}O_2$, which prevents lattice oxygen from participating in the reaction, thus avoiding the collapse of the structure. We proved that the Bi dopants could play a crucial role in not only reducing the energy barrier of the potential-determining step, but also delivering electrons to Ru sites, thereby alleviating the over-oxidation of Ru active sites and enhancing operation durability.

Introduction

As a significant route to develop green hydrogen energy, the water electrolysis technique attracts tremendous attention due to the cleanliness and sustainability to utilize renewable energy sources.[1–3] Compared to alkaline water electrolyzers with thick separating membranes, proton exchange membrane water electrolysis (PEMWE) electrolyzers are designed to be more compact,[2] only with a membrane thickness ranging from 20 to 300 μm.[4] PEMWE electrolyzers can achieve a high current density of over 2 A cm^{-2},[2,5] making them highly suitable for rapid response to intermittent renewable power sources.[6] Additionally, PEMWE electrolyzers can meet the energy conversion requirements at the terawatt (TW) scale and produce high-purity compressed hydrogen products.[2,7] Nevertheless, the development of PEM water electrolysis is largely constrained by the inferior stability and high overpotential of the anodic oxygen evolution reaction (OER) in harsh acidic media, which is due to its sluggish four-electron process.[8,9]

Recently, ruthenium and iridium oxides have been considered as acidic OER catalyst candidates for practical application of PEMWE electrolyzers.[10–12] In this regard, ruthenium is much cheaper than iridium (less than 10% of iridium) to meet the application in a wide range from industry to daily life.[13–15] However, enhancing the stability of ruthenium-based catalysts represents a significant challenge that currently needs to be addressed. The stability of Ru-based catalysts is predominantly limited by the formation of overoxidized Ru containing species, such as RuO_4, which is soluble and gradually leaches into the electrolyte during the OER process.[16] To simultaneously improve the catalytic activity and stability of Ru-based catalysts, various strategies, including doping with heterogeneous metal atoms,[17–24] strain engineering[25–27] and constructing a heterostructure,[28,29] have been extensively applied to achieve this goal. Although techniques such as impregnation or electrochemical deposition can produce highly dispersed single-atom catalysts with enhanced atomic efficiency, they may increase the complexity and cost of production. Surface modifications that involve organic molecules or metal ions can improve catalytic activity, yet they might adversely affect stability.[30,31] Among these techniques to improve the catalytic performance of Ru-based catalysts, the doping strategy is one of the most effective and facile methods

[a]State Key Laboratory of Chemical Resource Engineering, College of Chemistry, Beijing University of Chemical Technology, Beijing 100029, P. R. China. E-mail: wangfm@buct.edu.cn, sunxm@mail.buct.edu.cn, liyp@mail.buct.edu.cn
[b]Ocean Hydrogen Energy R&D Center, Research Institute of Tsinghua University in Shenzhen, Shenzhen, P. R. China

†Electronic supplementary information (ESI) available. See DOI: https://doi.org/10.1039/d4nr02745k

to boost the stability due to its ability to modify the electronic structure and surface properties of the catalyst. Furthermore, doping also enables the modulation of the acid–base properties and active sites on the catalyst surface, which makes it a powerful tool in enhancing the catalytic performance of Ru-based catalysts.[17–22,24,32]

Bismuth (Bi), known for its variable oxidation states (+3 and +5) and high redox potential, possesses promising potential in enhancing the valence state and stabilizing lattice structures. Bi possesses a remarkably low electronegativity (2.02), implying its reluctance to readily acquire electrons. Additionally, bismuth's relatively large atomic radius allows it to regulate the lattice structure of host materials through tensile strain during doping, further modulating their physical and chemical characteristics. Besides, bismuth is not only relatively non-toxic, which makes it environmentally friendly, but also inexpensive so as to reduce the use of the precious metal, thereby lowering overall costs. These unique properties of Bi make it a strong candidate for doping applications.

Herein, we successfully doped different ratios (x) of bismuth elements into the RuO_2 lattice by the sol–gel method to obtain $Bi_xRu_{1-x}O_2$ nanocrystals with the diameter of 6.5 ± 0.1 nm. X-ray photoelectron spectroscopy analysis on the $Bi_{0.05}Ru_{0.95}O_2$ sample demonstrates that the introduction of Bi atoms could regulate the valence state of Ru to be lower than +4. Then, the $Bi_{0.05}Ru_{0.95}O_2$ anode was evaluated in 0.5 M H_2SO_4 for OER and shows a low overpotential (203.5 mV) at a current density of 10 mA cm^{-2} and excellent stability (more than 300 h) at a current density of 100 mA cm^{-2} with a small decay rate (0.44 mV h^{-1}). We found that $Bi_xRu_{1-x}O_2$ electrocatalysts showed better performance than home-made RuO_2 (the corresponding overpotential is 227.8 mV, 183.3 h at 100 mA cm^{-2}) and commercial RuO_2 (403.0 mV, <5 h at 100 mA cm^{-2}) counterparts. Furthermore, theoretical calculations confirm that the OER occurring on the $Bi_{0.05}Ru_{0.95}O_2$ catalyst follows the adsorbate evolution mechanism (AEM) pathway so as to effectively suppress the participation of lattice oxygen. As a result, the strengthened M–O bonds in $Bi_{0.05}Ru_{0.95}O_2$ could prevent the formation of soluble high-valent Ru species for the robust OER process in acidic media.

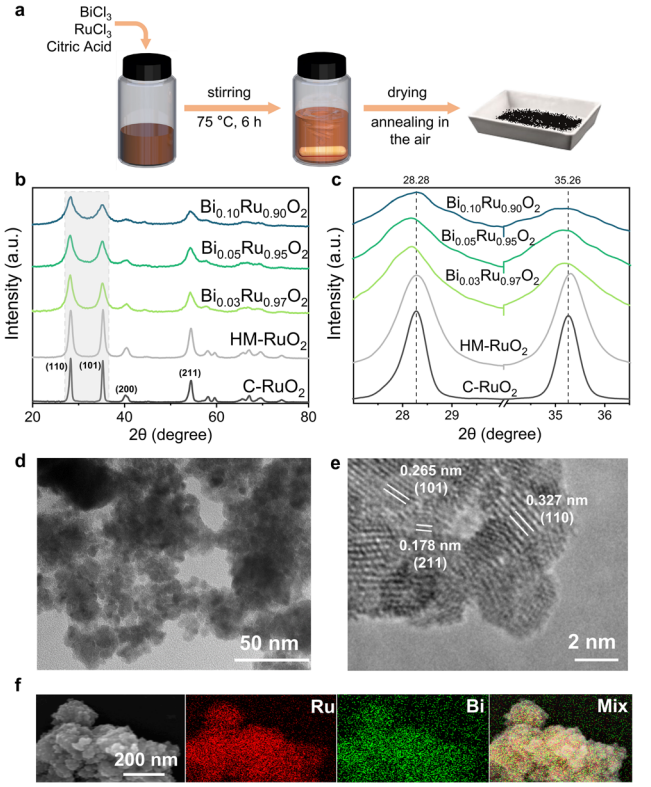

Fig. 1 Synthesis and structural characterization of the as-prepared $Bi_xRu_{1-x}O_2$. (a) Schematic of the synthesis of the $Bi_xRu_{1-x}O_2$ samples. (b and c) XRD patterns of the as-synthesized $Bi_xRu_{1-x}O_2$ (x = 0, 0.03, 0.05 and 0.10), HM–RuO_2 and C–RuO_2. The black dashed lines indicate the positions of the corresponding crystal plane peaks from C–RuO_2. (d) TEM image obtained from the $Bi_{0.05}Ru_{0.95}O_2$ sample. (e) HRTEM image of $Bi_{0.05}Ru_{0.95}O_2$. (f) SEM image and the corresponding EDS elemental mappings of the $Bi_{0.05}Ru_{0.95}O_2$ sample.

Experimental section

Materials synthesis

Different ratios of Bi atoms were introduced into the RuO_2 lattice to partially replace the Ru atom by the sol-gel method utilizing citric acid as the coordination agent in deionized water, as shown in Fig. 1a. In a typical synthesis, $BiCl_3$ was first pre-dissolved in 5 mL of 37% HCl and then added to a 5 mL aqueous solution of citric acid after adding ruthenium(III) nitrosyl nitrate (1.5% Ru w/v solution in H_2O). The above solution was continuously stirred for 6 hours at 75 °C in a closed system to obtain a sol–gel, which was then dried in air at 80 °C for about 10 h to obtain the powder. Finally, the collected powder was annealed at 400 °C for 5 h in air to obtain the $Bi_xRu_{1-x}O_2$ samples (x = 0.03, 0.05 and 0.10). In addition, homemade RuO_2 without element doping (HM-RuO_2) was synthesized by a similar synthesis procedure without adding $BiCl_3$ and the $Sb_{0.04}Ru_{0.96}O_2$ sample was also synthesized by a similar synthesis procedure through replacing $BiCl_3$ with $SbCl_3$.

Structural characterization

Scanning electron microscopy (SEM) images of various samples were obtained on a Zeiss SUPRA55 scanning electron microscope with Energy Dispersive Spectroscopy (EDS) operating at an accelerating voltage of 15.00 kV. Transmission Electron Microscopy (TEM) was carried out on a Hitachi HT7700 and High-Resolution Transmission Electron Microscopy (HR-TEM) was performed on a Thermo Electron ESCALAB250 XPS spectrometer. X-ray diffraction (XRD) patterns were recorded on a Bruker D2 Phaser diffractometer with Cu Kα radiation of 1.54184 Å at a scan rate slower than 2° min^{-1} in the 2θ range from 20 degrees to 80 degrees. X-ray photoelectron spectroscopy (XPS) measurements were carried out using an X-ray photoelectron spectrometer (Thermo Electron ESCALAB 250). We used adventitious carbon contami-

nation as a charge reference (284.8 eV) for XPS spectra and employed the software named Thermo Avantage to accurately fit XPS peaks.

Electrochemical measurements

To prepare the working electrode, 5 mg of various powder catalysts and 20 μL of Nafion 117 solution (5 wt%) were ultrasonicated in 1 mL of ethanol for more than 1 h to first produce a well-dispersed ink, and the prepared ink was drop-cast onto a carbon paper with an area of 1 × 1 cm^2, which was dried under infrared light to provide a catalyst loading of about 5 mg cm^{-2} (3.47 mg_{Ru} cm^{-2}). After this, the carbon paper was clamped onto the electrode holder. The electrochemical measurements on the different working electrodes were performed in 0.5 M H_2SO_4 electrolyte using a typical three-electrode system on an electrochemical station (CHI660E, Chenhua), with a Pt plate and a saturated calomel electrode (SCE) as the counter electrode and the reference electrode, respectively. Linear sweeping voltammograms (LSVs) were measured at a scan rate of 5 mV s^{-1} from 0.8 to 1.8 (V *vs.* SCE), which were converted to electrode potentials with respect to the reversible hydrogen electrode and undergone 100% *iR* correction. The electrochemical impedance spectroscopy (EIS) measurements were performed at 1.24 V in a frequency range from 10^5 to 1 Hz. To analyse the electrochemical active surface areas (ECSAs), the electrochemical double-layer capacitances (C_{dl}) were calculated using cyclic voltammetry (CV) curves recorded at different scan rates (5, 10, 15, 20, 25 and 30 mV s^{-1}) in the potential range of 0.6–0.8 (V *vs.* SCE). In a two-electrode system with a Pt plate as the counter electrode, chronopotentiometry curves were recorded at a current density of 100 mA cm^{-2} to evaluate the stability of the electrode. *In situ* Raman measurements were conducted in a 0.1 M $HClO_4$ solution, with the voltage ranging from 1.05 V to 1.32 V against the reversible hydrogen electrode reference electrode. The counter electrode was a platinum sheet electrode of 0.5 × 0.5 cm^2. The working electrode was prepared using the same catalyst loading and preparation methods as those employed in the three-electrode system tests.

DFT calculations

Given the fact of the dispersion of Bi atoms, a rutile $Bi_2Ru_{34}O_{72}$ model was established to simulate the $Bi_{0.05}Ru_{0.95}O_2$ catalyst (Fig. S1†). Density functional theory (DFT) calculations were performed on the $Bi_2Ru_{34}O_{72}$ model using the Vienna *Ab initio* Simulation Package (VASP) to probe the electronic and structural properties of $Bi_{0.05}Ru_{0.95}O_2$.[33,34] These calculations were performed using the projector-augmented wave (PAW) method in conjunction with the Perdew–Burke–Ernzerhof (PBE) generalized gradient approximation (GGA) to model the electronic interactions within the system.[35–37] A similar structure with oxygen vacancies (Bi–O_v–RuO_2) and a rutile pure RuO_2 model (RuO_2) were also established as a comparison (Fig. S2 and S3†). In our research, the (110) surface of rutile phase ruthenium dioxide (RuO_2) has been selected for our DFT calculations.[38,39] All structures were spin polarized, and all atoms were fully relaxed with an energy convergence tolerance of 10^{-5} eV per atom, and the final force on each atom was less than 0.05 eV $Å^{-1}$. When calculating the absorption free energy change of intermediates, we followed the steps shown in Fig. 4a and b and fixed the bottom three layers of atoms in the cell.

We employed a Monkhorst–Pack *k*-point grid with sampling parameters of 4 × 3 × 1 to effectively sample the Brillouin zone.[40] A high-energy cutoff value of 500 eV was selected for the plane-wave basis set for more accurate calculations. To further enhance the accuracy of our calculation, we optimized the geometric and electronic structures using the DFT + *U* method with a Hubbard *U* value of 2.0 for Ru.[41,42] See the ESI† for more details.

Results and discussion

Materials characterization

As shown in Fig. 1a, $Bi_xRu_{1-x}O_2$ samples (x = 0, 0.03, 0.05 and 0.10) were prepared using a sol–gel method (see the Experimental section for details). X-ray diffraction (XRD) patterns of these samples (Fig. 1b) show that the as-prepared $Bi_xRu_{1-x}O_2$ samples possess the same crystal phase as rutile RuO_2 (JCPDS file no. 43-1027) without any evidence for impurity from Bi_2O_3, suggesting the successful Bi substitution of the Ru site in RuO_2 crystals. The enlarged XRD pattern (Fig. 1c) reveals that shifts towards lower angles for the (110) and (101) peaks compared to those of C–RuO_2 are observed in the $Bi_xRu_{1-x}O_2$ samples due to the Bi element substitution. The TEM images in Fig. 1d and Fig. S4–S6† confirm that the crystallite size of 6.5 ± 0.1 nm for the $Bi_{0.05}Ru_{0.95}O_2$ sample is significantly smaller than those of C–RuO_2 (>50 nm) and HM–RuO_2 (12.9 ± 0.2 nm), consistent with the XRD patterns in Fig. 1b. Furthermore, compared with that of C–RuO_2 (Fig. S7†), the HRTEM image of $Bi_{0.05}Ru_{0.95}O_2$ in Fig. 1e shows slightly enlarged lattice fringes of 0.327 nm and 0.265 nm for the (110) and (101) crystal planes, respectively, which are larger than those (0.317 nm and 0.250 nm) for C–RuO_2, further confirming the successful introduction of larger radius Bi atoms into the lattice structure of rutile ruthenium dioxide. The SEM images in Fig. 1f and Fig. S8† show that the $Bi_xRu_{1-x}O_2$ and HM–RuO_2 samples exhibit a rough surface with smaller particle sizes compared to that of C–RuO_2 (Fig. S9†). The corresponding elemental mapping of $Bi_{0.05}Ru_{0.95}O_2$ showed a uniform distribution of Ru and Bi elements. Due to the limited oxidation states of bismuth (Bi) at +3 and +5, it is not favorable for the formation of a solid solution that matches the coordination number of the rutile phase, so a relatively low doping concentration was selected. The elemental ratios of Bi in different samples were confirmed as 3 at%, 5 at%, and 10 at% in Table S1.†

To delve into the valence state of Ru and Bi elements in the samples, we conducted a thorough XPS characterization. As shown in Fig. 2a, the XPS spectra clearly show the characteristic peaks of various elements, including Bi, Ru and O. Subsequently, the fitting of the Ru 3p peak (Fig. 2b) of

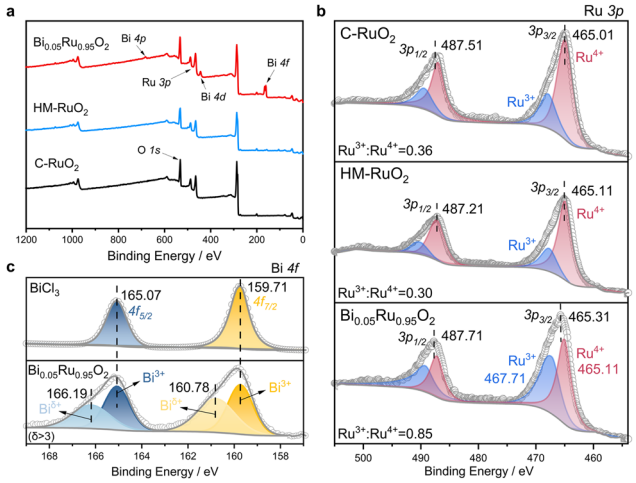

Fig. 2 XPS analysis of the $Bi_{0.05}Ru_{0.95}O_2$ sample. (a) XPS survey spectra of $Bi_{0.05}Ru_{0.95}O_2$, HM–RuO_2 and C–RuO_2. (b) Ru 3p XPS spectra of $Bi_{0.05}Ru_{0.95}O_2$, HM–RuO_2 and C–RuO_2. (c) Bi 4f XPS spectra of $Bi_{0.05}Ru_{0.95}O_2$ and $BiCl_3$.

$Bi_{0.05}Ru_{0.95}O_2$ shows two peaks located at 465.31 and 487.71 eV corresponding to Ru $3p_{3/2}$ and Ru $3p_{1/2}$. A slight shift of 0.2 eV to the higher binding energy than that of HM–RuO_2 and 0.3 eV to the higher binding energy than that of commercial RuO_2 (C–RuO_2) were observed in the $Bi_{0.05}Ru_{0.95}O_2$ sample, indicating a decrease in the oxidation state of Ru sites after introducing Bi atoms. The Ru $3p_{3/2}$ peak can be deconvoluted into two peaks centred at 465.11 eV and 467.71 eV, which are assigned to the Ru^{4+} and Ru^{3+} species, respectively. Compared to that of HM–RuO_2, the ratio of Ru^{3+}/Ru^{4+} in $Bi_{0.05}Ru_{0.95}O_2$ was increased from 0.30 to 0.85, implying the reduction of the Ru valence state. The deconvolution of the Bi 4f orbital reveals the presence of a higher valence state than +3, compared with that of the commercial $BiCl_3$ reference sample. Hence, it could be concluded that the electron transferred from Bi to nearby Ru sites through bridge oxygen to create more low valent Ru sites, which would probably modulate the adsorption of oxygen intermediates and improve the OER catalytic activity and stability. Additionally, the O 1s XPS spectra could be deconvoluted into lattice oxygen (O_L), metal–OH bond (M–OH), oxygen defect (O_V), and adsorbed water (O_{ads}) peaks, respectively (Fig. S10†).[32] It can be observed that the oxygen defect peak ratio in $Bi_{0.05}Ru_{0.95}O_2$ is 0.23, higher than that of C–RuO_2 (0.16) and higher than that of HM–RuO_2 (0.21), indicating the higher activity (Table S2†).

Acidic OER performance of $Bi_xRu_{1-x}O_2$ electrocatalysts

To delve into the catalytic performance of $Bi_xRu_{1-x}O_2$ towards the oxygen evolution reaction (OER) under acidic conditions, a comprehensive series of electrochemical tests were conducted. As a comparison, C–RuO_2 and HM–RuO_2 were also tested under the same conditions. Firstly, a linear sweep voltammetry (LSV) study was conducted in a traditional three-electrode system using 0.5 M H_2SO_4 (see the Experimental section for the details), as presented in Fig. 3a, which reveals that the $Bi_{0.05}Ru_{0.95}O_2$ electrode requires an overpotential of 203.5 mV to deliver a current density of 10 mA cm^{-2}, which is much lower than those of C–RuO_2 (403.0 mV), HM–RuO_2 (227.8 mV), $Bi_{0.03}Ru_{0.97}O_2$ (213.2 mV), and $Bi_{0.10}Ru_{0.90}O_2$ (207.8 mV) electrodes. This result indicates the significant positive role of Bi doping in the electrochemical activity (Table S3†). The ECSA values of the various electrodes (Table S4†) were investigated through obtaining the C_{dl} values in Fig. S11 and S12,† indicating that Bi doping can affect the morphology of RuO_2 positively and thereby increase the number of active sites. The ECSA comparison of the various electrodes (Table S4†) and the accordingly normalized polarization curves in Fig. S13† indicate that Bi doping can affect the morphology of RuO_2 positively and thereby increase the number of active sites. Furthermore, the significant enhancement in the specific activity of $Bi_xRu_{1-x}O_2$ (lower than 242.4 mV at 10 mA $cm^{-2}_{normalized}$) compared to HM–RuO_2 (254 mV at 10 mA $cm^{-2}_{normalized}$) and C–RuO_2 (257 mV at 10 mA $cm^{-2}_{normalized}$) suggests that the important

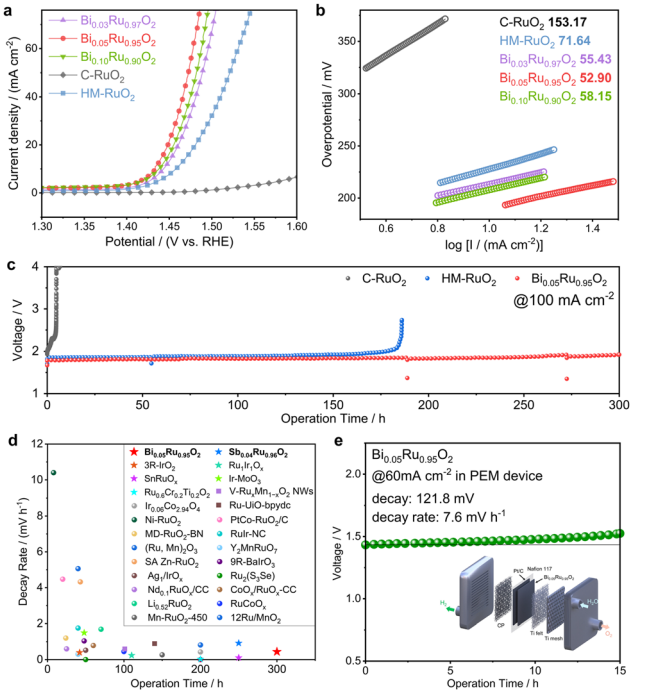

Fig. 3 Electrocatalytic performances of the $Bi_xRu_{1-x}O_2$ catalysts towards the OER. (a) Polarization curves in 0.5 M H_2SO_4 electrolyte at a scan rate of 5 mV s^{-1} for the $Bi_xRu_{1-x}O_2$, HM–RuO_2 and C–RuO_2 electrodes. (b) Corresponding Tafel plots of the $Bi_xRu_{1-x}O_2$, HM–RuO_2 and C–RuO_2 electrodes. (c) Chronopotentiometry tests of $Bi_{0.05}Ru_{0.95}O_2$, HM–RuO_2 and C–RuO_2 at 100 mA cm^{-2} in 0.5 M H_2SO_4. (d) Comparison of the operation time (h) and decay rate (mV h^{-1}) between the $Bi_{0.05}Ru_{0.95}O_2$, $Sb_{0.04}Ru_{0.96}O_2$ and reported Ir- and Ru-based catalysts at their reported current densities. The star represents stability at a current density of 100 mA cm^{-2}, the square represents stability at 50 mA cm^{-2}, and the circle represents stability at 10 mA cm^{-2}. (e) Chronopotentiometry curve of the PEM electrolyzer at 60 mA cm^{-2} using $Bi_{0.05}Ru_{0.95}O_2$ as the anode catalyst in pure water at 80 °C. The inset shows the device diagram.

role of Bi doping in improving the activity of ruthenium dioxide. The Tafel plot extracted from the polarization curve in Fig. 3b shows that the Tafel slopes of $Bi_xRu_{1-x}O_2$, with values ranging from 52.90 to 58.15 mV dec^{-1} for different x values are significantly lower than those of C–RuO_2 (153.17 mV dec^{-1}) and HM–RuO_2 (71.64 mV dec^{-1}), indicating the faster kinetics for OER and accelerating electron transfer. The low Tafel slope of 52.90 mV dec^{-1} on the $Bi_{0.05}Ru_{0.95}O_2$ electrocatalyst, compared with other reported catalysts in Table S5,† suggests the faster electron transfer kinetics. The electrochemical impedance spectroscopy (EIS) result further reveals that $Bi_{0.05}Ru_{0.95}O_2$ showed a smaller solution resistance value (0.898 Ω) than those of HM–RuO_2 and C–RuO_2 (2.316 Ω and 1.328 Ω, respectively) (Fig. S14†), indicating a superior electrochemical process and providing further evidence of the important role of Bi doping in RuO_2.

Catalyst stability at a high current density is also crucial for applying an acidic OER electrode to the industrial scale. In this regard, we investigated and compared the stability of the as-synthesized catalysts and C–RuO_2 by chronopotentiometry (CP) measurements at a high current density of 100 mA cm^{-2} (Fig. 3c and Fig. S15†). Dramatically, decay is observed within 5 hour testing on the C–RuO_2 electrodes under 100 mA cm^{-2}. Notably, the $Bi_{0.05}Ru_{0.95}O_2$ electrode could be continuously operated at 100 mA cm^{-2} for more than 300 h with a low decay rate of 0.44 mV h^{-1}, outperforming the HM–RuO_2 electrodes (242 mV decay within 183.3 h) and presenting a 60-fold improvement compared to C–RuO_2, which shows that Bi element incorporated *via* the sol–gel method is beneficial for improving the activity and stability. Based on the results presented in Fig. S16,† along with the dependence of TOF values on dopant concentrations for various catalysts as illustrated in Fig. S17,† the cumulative evidence conclusively shows that an optimal dopant concentration can enhance the number of active sites for OER, thereby increasing the electrochemical activity of the material. This, in turn, leads to simultaneous improvements in both reactivity and stability. To further evaluate the stability of $Bi_{0.05}Ru_{0.95}O_2$, we retested the electrode after it had been running at 100 mA cm^{-2} for 188 hours (Fig. S18†). The EIS and LSV curves remained largely unchanged after 188 h stability testing, demonstrating the catalyst's remarkable stability (Fig. S19 and S20†). Fig. 3d shows the comparison of the stability of the $Bi_{0.05}Ru_{0.95}O_2$ catalyst with other reported ones, clearly demonstrating its promising stability for acidic OER (Fig. S21 and Table S6†).

In situ Raman measurements were conducted in a 0.1 M $HClO_4$ solution, with the voltage ranging from 1.05 V to 1.32 V against the reversible hydrogen electrode reference electrode (Fig. S22†). In the potential range of 1.05 V–1.32 V (*vs.* RHE), the intensity of the 457 cm^{-1} peak, attributed to hydrated RuO_2,[46] gradually increases and then remains unchanged, suggesting an enhanced adsorption of water molecules. In contrast, the 515 cm^{-1} peak remains stably unchanged in intensity and position within the potential window of 1.05 V–1.24 V, demonstrating that the surface chemical state corresponding to the E_g vibrational mode does not undergo significant alteration within this range.[47] Besides, when the potential increases, its disappearance at potentials higher than 1.26 V may suggest surface reconstruction, potentially involving a transition from a crystalline to an amorphous state. Furthermore, the peak corresponding to the A_{1g} vibrational mode is proven to remain unchanged within the potential range of 1.05 V–1.26 V, demonstrating the relative stability of the corresponding chemical bonds or structures.[47] Upon increasing the potential to between 1.28 V and 1.32 V, the peak red shifts slightly to 626 cm^{-1}, suggesting a small increase in bond length and a decrease in oxidation state.[47,48]

Given the excellent electrocatalytic performance of the $Bi_{0.05}Ru_{0.95}O_2$ catalyst for acidic OER in a two-electrode system, we further performed chronopotentiometry tests in a PEM electrolyzer device (insert in Fig. 3e) with $Bi_{0.05}Ru_{0.95}O_2$ (10 mg cm^{-2}) as the anodic catalyst and Pt/C (40 wt%, 10 mg cm^{-2}) as the cathodic catalyst. Membrane electrode assemblies (MEAs) were prepared by the catalyst coating method (CCM), *i.e.*, spraying catalyst ink on a 1 × 1 cm^2 Nafion 117 membrane. The test was performed at atmospheric pressure and 80 °C with liquid water injected on the anode side of the cell. The PEM electrolyzer using the $Bi_{0.05}Ru_{0.95}O_2$ catalyst could operate at 60 mA cm^{-2} for more than 15 hours with the initial cell voltage less than 1.5 V (Fig. 3e).

In addition, the antimony (Sb)-doped RuO_2 (*i.e.*, $Sb_xRu_{1-x}O_2$) electrocatalyst for acidic OER was also explored. For comparison with the $Bi_{0.05}Ru_{0.95}O_2$ sample, the content of Sb (x) was regulated to around 0.05. The $Sb_{0.04}Ru_{0.96}O_2$ sample was synthesized through the same method and the Sb content in $Sb_xRu_{1-x}O_2$ was confirmed through EDS spectral analysis (Table S7†). As shown in Fig. S23–S25,† the XRD pattern, SEM image and EDS mapping analysis of the $Sb_{0.04}Ru_{0.96}O_2$ sample showed that Sb was successfully doped into the rutile RuO_2 lattice and exhibits a similar morphology to that of $Bi_{0.05}Ru_{0.95}O_2$. Specifically, $Sb_{0.04}Ru_{0.96}O_2$ achieved an overpotential of 285.2 mV at 10 mA cm^{-2} (Fig. S26†) and could operate stably at 100 mA cm^{-2} for 250 hours (Fig. S27†), demonstrating a slightly inferior performance for acidic OER than that of the $Bi_{0.05}Ru_{0.95}O_2$ electrocatalyst.

Theoretical calculations

To gain a deeper understanding of the electronic structure and properties modulated by Bi doping in ruthenium dioxide, we performed density functional theory (DFT) calculations. These calculations provide insights into the electronic structure and catalytic mechanism at the fundamental level.

There are typically two mechanisms in electrocatalysis: the adsorption evolution mechanism (AEM) (Fig. 4a) and the lattice oxygen mediated mechanism (LOM) (Fig. 4b). In the LOM, lattice oxygen atoms located at two adjacent sites directly couples to form an O–O bond, leading to the release of oxygen. Although not requiring the formation of intermediate adsorbed species like *OOH, which may lead to higher activity, this process involves lattice oxygen, thereby elevating the risk of structural collapse and potentially resulting in inferior

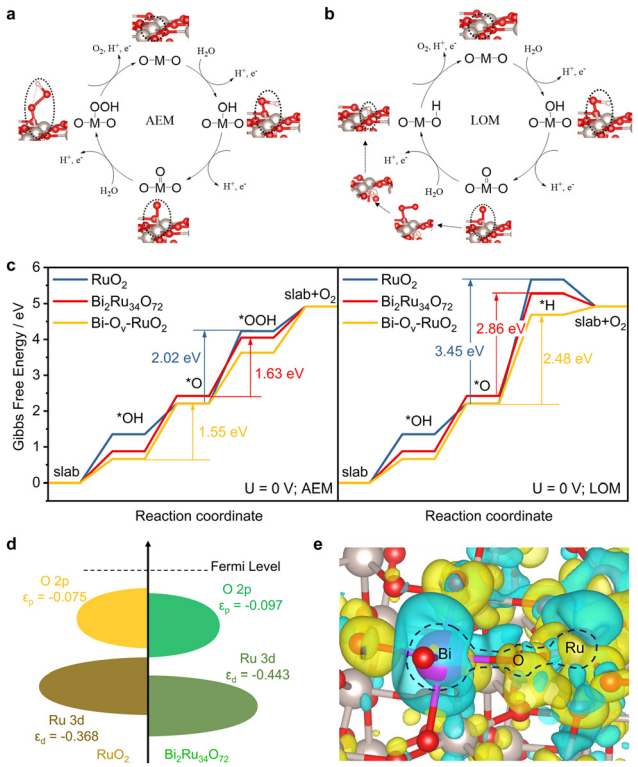

Fig. 4 DFT calculation results. (a) Diagram of the AEM for the acidic OER. (b) Diagram of the LOM for the acidic OER. (c) Gibbs free energy diagram for the acidic OER *via* the AEM (left panel) and the LOM (right panel) of Bi–O_v–RuO_2 (yellow line), $Bi_2Ru_{34}O_{72}$ (red line) and RuO_2 (blue line). Values with different colors represent the energy barrier of the corresponding mechanism for Bi–O_v–RuO_2, $Bi_2Ru_{34}O_{72}$ and RuO_2. (d) Calculated positions of the Ru 3d band center and O 2p band center for the RuO_2 model and the $Bi_{34}Ru_2O_{72}$ model (unit: eV). (e) Charge density difference plot of $Bi_2Ru_{34}O_{72}$. The blue and yellow shaded areas show the electron density depletion and accumulation, respectively.

stability.[12,43] To explore the main mechanism occurring on $Bi_xRu_{1-x}O_2$, we calculated the Gibbs free energies of various intermediates on $Bi_2Ru_{34}O_{72}$ and RuO_2 involving in the AEM and LOM. As shown in Fig. 4c, the Gibbs energy change for the LOM (2.86 eV) is higher than that for the AEM (1.63 eV), which indicates that the AEM is more favourable (Table S8†), which is consistent with the pH dependency experiment result (Fig. S28†).[44] The free energy diagram showed that the potential-determining steps (PDSs) of both RuO_2 and $Bi_2Ru_{34}O_{72}$ were the formation of OOH* from O*. The calculated Gibbs energy change of the PDS of $Bi_2Ru_{34}O_2$ was 1.63 eV, lower than that of RuO_2 (2.02 eV), demonstrating the relatively lower overpotential and higher activity of $Bi_2Ru_{34}O_{72}$. Additionally, theoretical calculations were also conducted on the Gibbs free energy diagram for OER *via* the AEM and the LOM of the Bi–O_v–RuO_2 structure containing oxygen vacancies. In this case, to guarantee a homogeneous distribution of oxygen vacancies, three randomly selected types of oxygen atoms were removed to simulate the oxygen vacancy contained structure, and the following structural optimization providing a stable configuration was screened and is depicted in Fig. S3.† Clearly, Fig. 4c shows a notable decrease in the energy barrier (1.55 eV) for theoretical overpotential for the oxygen evolution reaction (OER) under both AEM and LOM pathways, indicating the OER process following the AEM pathway with superior stability.

As depicted in Fig. 4d, the Ru 3d band center of $Bi_{34}Ru_2O_{72}$ is located at −0.443 eV, which is significantly shifted further away from the Fermi level compared to the −0.368 eV of pure ruthenium dioxide (RuO_2). This shift in the d-band center of $Bi_{34}Ru_2O_{72}$ results in an enhanced adsorption of *OOH, which can help to balance the four-electron process and lead to the enhancement of the reaction activity.[45] In addition, the charge distribution between Bi and Ru also played an important role in promoting the OER. Charge density difference analysis has unveiled that the presence of Bi atoms significantly alters the charge distribution on the surface of $Bi_2Ru_{34}O_{72}$, promoting the accumulation of charge at the Ru sites, thereby enhancing the overall stability of the catalyst (Fig. 4e). Furthermore, we calculated the demetalisation energies of surface Ru sites in Bi–O_v–RuO_2, $Bi_2Ru_{34}O_{72}$ and RuO_2. As shown in Fig. S29,† the demetalisation energies of $Bi_2Ru_{34}O_{72}$ and Bi–O_v–RuO_2 are 3.89 eV and 4.02 eV, respectively, much higher than that of RuO_2 (3.29 eV), indicating a greater resistance to dissolution. This finding consists with our experimental results and provides strong evidence that Bi doping effectively enhances the stability of the catalyst. In summary, by doping Bi into RuO_2, the electronic structure of RuO_2 and the adsorption energy of reaction intermediates were adjusted, which is beneficial for stabilization of RuO_2 and protects Ru sites from over-oxidation during OER catalysis at a high current density.

Conclusions

To sum up, this work demonstrates the promising potential of introducing bismuth (Bi) element to improve the activity and stability of rutile RuO_2 for acidic OER. The activity and stability of RuO_2 could be enhanced through appropriate Bi substitution. The $Bi_{0.05}Ru_{0.95}O_2$ electrocatalyst demonstrates a low overpotential of 203.5 mV at 10 mA cm^{-2} and excellent stability for over 300 h under a high water-splitting current of 100 mA cm^{-2} in 0.5 M H_2SO_4. Experimental and theoretical investigations verified that the OER follows the adsorbate evolving mechanism (AEM) on $Bi_{0.05}Ru_{0.95}O_2$ and the energy barrier of the potential-determining step is effectively reduced after introducing Bi dopants. Overall, this study lays a foundation for efficient energy conversion and contributes to the ongoing effort to develop effective and sustainable electrocatalysts for proton exchange membrane water electrolyzers and green hydrogen energy.

Author contributions

F. M. Wang, X. M. Sun, and Y. P. Li conceived and supervised the research. S. Y. Chen and H. Liu conducted the sample synthesis, characterization, electrochemical measurements, and

data analysis. S. Y. Chen, W. H. Xu, and A. Q. Cao performed the DFT calculations. M. G. Sendeku revised the manuscript. S. Y. Chen, B. C. Yuan, and F. M. Wang wrote the manuscript with inputs from all authors.

Data availability

The data supporting this article have been included as part of the ESI.†

Conflicts of interest

There are no conflicts to declare.

Acknowledgements

This work was supported by the National Key Research and Development Project (2023YFB4005100), the National Natural Science Foundation of China (No. 22179029), the Fundamental Research Funds for the Central Universities (buctrc202324), the Young Elite Scientists Sponsorship Program by CAST (2023QNRC001) and the Young Elite Scientists Sponsorship Program by BAST (BYESS2023093).

References

1 L. Quan, H. Jiang, G. Mei, Y. Sun and B. You, *Chem. Rev.*, 2024, **124**, 3694–3812.
2 R. T. Liu, Z. L. Xu, F. M. Li, F. Y. Chen, J. Y. Yu, Y. Yan, Y. Chen and B. Y. Xia, *Chem. Soc. Rev.*, 2023, **52**, 5652–5683.
3 M. Chen, N. Kitiphatpiboon, C. Feng, A. Abudula, Y. Ma and G. Guan, *eScience*, 2023, **3**, 100111.
4 L. An, C. Wei, M. Lu, H. Liu, Y. Chen, G. G. Scherer, A. C. Fisher, P. Xi, Z. J. Xu and C.-H. Yan, *Adv. Mater.*, 2021, **33**, 2006328.
5 L. A. Cohen, M. S. Weimer, K. Yim, J. Jin, D. V. Fraga Alvarez, A. A. Dameron, C. B. Capuano, R. J. Ouimet, S. Fortiner and D. V. Esposito, *ACS Energy Lett.*, 2024, **9**, 1624–1632.
6 S. Stiber, N. Sata, T. Morawietz, S. A. Ansar, T. Jahnke, J. K. Lee, A. Bazylak, A. Fallisch, A. S. Gago and K. A. Friedrich, *Energy Environ. Sci.*, 2022, **15**, 109–122.
7 A. Kocalmis Bilhan, *Int. J. Hydrogen Energy*, 2024, **75**, 415–427.
8 N. T. Suen, S. F. Hung, Q. Quan, N. Zhang, Y. J. Xu and H. M. Chen, *Chem. Soc. Rev.*, 2017, **46**, 337–365.
9 J. Bai, W. Zhou, J. Xu, P. Zhou, Y. Deng, M. Xiang, D. Xiang and Y. Su, *Molecules*, 2024, **29**, 537.
10 J. Rossmeisl, A. Logadottir and J. K. Nørskov, *Chem. Phys.*, 2005, **319**, 178–184.
11 K. Klyukin, A. Zagalskaya and V. Alexandrov, *J. Phys. Chem. C*, 2019, **123**, 22151–22157.
12 N. Zhang and Y. Chai, *Energy Environ. Sci.*, 2021, **14**, 4647–4671.
13 Y. Zheng, Y. Jiao, Y. Zhu, L. H. Li, Y. Han, Y. Chen, M. Jaroniec and S. Z. Qiao, *J. Am. Chem. Soc.*, 2016, **138**, 16174–16181.
14 V. Yadav, Megha, P. Sen and M. M. Shaijumon, *J. Mater. Chem. A*, 2024, **12**, 5319–5330.
15 C. Li, L. Chen, D. Dou, H. Wang, Q. Zhao and Y. Cong, *Ionics*, 2023, **29**, 4987–5001.
16 F. Y. Chen, Z. Y. Wu, Z. Adler and H. T. Wang, *Joule*, 2021, **5**, 1704–1731.
17 H. Liu, Z. Zhang, J. Fang, M. Li, M. G. Sendeku, X. Wang, H. Wu, Y. Li, J. Ge, Z. Zhuang, D. Zhou, Y. Kuang and X. Sun, *Joule*, 2023, **7**, 558–573.
18 Z. Y. Wu, F. Y. Chen, B. Li, S. W. Yu, Y. Z. Finfrock, D. M. Meira, Q. Q. Yan, P. Zhu, M. X. Chen, T. W. Song, Z. Yin, H. W. Liang, S. Zhang, G. Wang and H. Wang, *Nat. Mater.*, 2023, **22**, 100–108.
19 R. Madhu, A. Karmakar, S. Kumaravel, S. S. Sankar, K. Bera, S. Nagappan, H. N. Dhandapani and S. Kundu, *ACS Appl. Mater. Interfaces*, 2022, **14**, 1077–1091.
20 D. Zhang, M. Li, X. Yong, H. Song, G. I. N. Waterhouse, Y. Yi, B. Xue, D. Zhang, B. Liu and S. Lu, *Nat. Commun.*, 2023, **14**, 2517.
21 Y. Wang, R. Yang, Y. Ding, B. Zhang, H. Li, B. Bai, M. Li, Y. Cui, J. Xiao and Z. S. Wu, *Nat. Commun.*, 2023, **14**, 1412.
22 S. Chen, H. Huang, P. Jiang, K. Yang, J. Diao, S. Gong, S. Liu, M. Huang, H. Wang and Q. Chen, *ACS Catal.*, 2019, **10**, 1152–1160.
23 T. Zhang, J. Li, Z. Qin, C. Li, H. Gao, F. Zhao and H. Ma, *Chem. Eng. J.*, 2021, **421**, 129436.
24 H. Jin, X. Liu, P. An, C. Tang, H. Yu, Q. Zhang, H. J. Peng, L. Gu, Y. Zheng, T. Song, K. Davey, U. Paik, J. Dong and S. Z. Qiao, *Nat. Commun.*, 2023, **14**, 354.
25 Y. Qin, T. Yu, S. Deng, X. Y. Zhou, D. Lin, Q. Zhang, Z. Jin, D. Zhang, Y. B. He, H. J. Qiu, L. He, F. Kang, K. Li and T. Y. Zhang, *Nat. Commun.*, 2022, **13**, 3784.
26 Y. Yao, S. Hu, W. Chen, Z.-Q. Huang, W. Wei, T. Yao, R. Liu, K. Zang, X. Wang, G. Wu, W. Yuan, T. Yuan, B. Zhu, W. Liu, Z. Li, D. He, Z. Xue, Y. Wang, X. Zheng, J. Dong, C.-R. Chang, Y. Chen, X. Hong, J. Luo, S. Wei, W.-X. Li, P. Strasser, Y. Wu and Y. Li, *Nat. Catal.*, 2019, **2**, 304–313.
27 Q. Wang, H. Liu, B. He, J. Qi, D. Wang, H. Xu, N. Zhang, J. Wang, Y. Chen, Z. Wang, Z. Wang, X. Qi, L. Zheng, M. Feng, W. Lü and S. Yan, *Appl. Catal., B*, 2022, **317**, 121781.
28 L. Ai, Y. Wang, Y. Luo, Y. Tian, S. Yang, M. Chen and J. Jiang, *J. Alloys Compd.*, 2022, **902**, 163787.
29 K. Huang, C. Lin, G. Yu, P. Du, X. Xie, X. He, Z. Zheng, N. Sun, H. Tang, X. Li, M. Lei and H. Wu, *Adv. Funct. Mater.*, 2023, **33**, 2211102.
30 A. R. Poerwoprajitno, L. Gloag, T. M. Benedetti, S. Cheong, J. Watt, D. L. Huber, J. J. Gooding and R. D. Tilley, *Small*, 2019, **15**, 1804577.

31 L. Deng, S.-F. Hung, Z.-Y. Lin, Y. Zhang, C. Zhang, Y. Hao, S. Liu, C.-H. Kuo, H.-Y. Chen, J. Peng, J. Wang and S. Peng, *Adv. Mater.*, 2023, **35**, 2305939.
32 Y. Wu, R. Yao, Q. Zhao, J. Li and G. Liu, *Chem. Eng. J.*, 2022, **439**, 135699.
33 G. Kresse and J. Furthmüller, *Phys. Rev. B: Condens. Matter Mater. Phys.*, 1996, **54**, 11169–11186.
34 G. Kresse and J. Furthmüller, *Comput. Mater. Sci.*, 1996, **6**, 15–50.
35 P. E. Blöchl, *Phys. Rev. B: Condens. Matter Mater. Phys.*, 1994, **50**, 17953–17979.
36 G. Kresse and D. Joubert, *Phys. Rev. B: Condens. Matter Mater. Phys.*, 1999, **59**, 1758–1775.
37 J. P. Perdew, J. A. Chevary, S. H. Vosko, K. A. Jackson, M. R. Pederson, D. J. Singh and C. Fiolhais, *Phys. Rev. B: Condens. Matter Mater. Phys.*, 1992, **46**, 6671–6687.
38 G. Novell-Leruth, G. Carchini and N. Lopez, *J. Chem. Phys.*, 2013, **138**, 194706.
39 Y. Lee, J. Suntivich, K. J. May, E. E. Perry and Y. Shao-Horn, *J. Phys. Chem. Lett.*, 2012, **3**, 399–404.
40 J. D. Pack and H. J. Monkhorst, *Phys. Rev. B: Solid State*, 1977, **16**, 1748–1749.
41 V. V. Anisimov, J. Zaanen and O. K. Andersen, *Phys. Rev. B: Condens. Matter Mater. Phys.*, 1991, **44**, 943–954.
42 H. C. Yang, B. C. Gong, K. Liu and Z. Y. Lu, *J. Phys.: Condens.Matter*, 2019, **31**, 025803.
43 S. Liu, Y. Chang, N. He, S. Zhu, L. Wang and X. Liu, *ACS Appl. Mater. Interfaces*, 2023, **15**, 20563–20570.
44 M. T. M. Koper, *Chem. Sci.*, 2013, **4**, 2710–2723.
45 G. Chen, R. Lu, C. Ma, X. Zhang, Z. Wang, Y. Xiong and Y. Han, *Angew. Chem., Int. Ed.*, 2024, e202411603, DOI: **10.1002/anie.202411603**.
46 W. Li, R. Zhou, X. Wang, L. Hu, X. Chen, P. Guan, X. Zhang, H. Zhang, J. Dong, Z. Tian and J. Li, *J. Catal.*, 2021, **400**, 367–371.
47 W. Gou, S. Zhang, Y. Wang, X. Tan, L. Liao, Z. Qi, M. Xie, Y. Ma, Y. Su and Y. Qu, *Energy Environ. Sci.*, 2024, DOI: **10.1039/D4EE02549K**.
48 Z. Niu, Z. Lu, Z. QIao, S. Wang, X. Cao, X. Chen, J. Yun, L. Zheng and D. Cao, *Adv. Mater.*, 2024, **36**, e2310690.